X-ray fluorescent CT imaging of cerebral uptake of stable-iodine perfusion agent iodoamphetamine analog IMP in mice

doi: 10.1107/S0909049508031853

Journal of
Synchrotron Radiation

ISSN 0909-0495

Received 8 August 2008
Accepted 3 October 2008

X-ray fluorescent CT imaging of cerebral uptake of stable-iodine perfusion agent iodoamphetamine analog IMP in mice

Tohoru Takeda,[a]* Jin Wu,[a] Thet-Thet-Lwin,[a] Qingkai Huo,[b] Tetsuya Yuasa,[b] Kazuyuki Hyodo,[c] F. Avraham Dilmanian[d] and Takao Akatsuka[b]

[a]Graduate School of Comprehensive Human Sciences, University of Tsukuba, Tsukuba-shi, Ibaraki 305-8575, Japan, [b]Graduate School of Science and Engineering, Yamagata University, Yonezawa-shi, Yamagata 992-8510, Japan, [c]National Laboratory for High Energy Physics, Tsukuba-shi, Ibaraki 305-0801, Japan, and [d]Medical Department, Brookhaven National Laboratory, Upton, NY 11973, USA. E-mail: ttakeda@md.tsukuba.ac.jp

Using X-ray fluorescent computed tomography (XFCT), the *in vivo* and *ex vivo* cerebral distribution of a stable-iodine-labeled cerebral perfusion agent, iodoamphetamine analog (^{127}I-IMP), has been recorded in the brains of mice. *In vivo* cerebral perfusion in the cortex, hippocampus and thalamus was depicted at 0.5 mm in-plane spatial resolution. *Ex vivo* XFCT images at 0.25 mm in-plane spatial resolution allowed the visualisation of the detailed structures of these regions. The quality of the XFCT image of the hippocampus was comparable with the ^{125}I-IMP autoradiogram. These results highlight the sensitivity of XFCT and its considerable potential to evaluate cerebral perfusion in small animals without using radioactive agents.

Keywords: X-ray fluorescent CT; fluorescent X-ray; molecular imaging; cerebral perfusion; IMP.

1. Introduction

Molecular imaging is a vital tool in evaluating various disorders, such as Alzheimer's disease, Parkinson's disease, ischemic heart disease, cardiomyopathy and cancer (Chatziioannou, 2002; Herschman, 2003). Recent advances in genetic engineering have generated rodent models of human diseases that afford important clues to their causes, diagnoses and treatment. *In vivo* biochemical processes in small animals have been visualized *via* micro positron-emission tomography (micro-PET) (Chatziioannou, 2002; Herschman, 2003; Yang *et al.*, 2004) and micro single-photon-emission computed tomography (micro-SPECT) (Acton & Kung, 2003; Beekman *et al.*, 2005; Madsen, 2007). However, both PET and SPECT studies necessitate the use of radionuclide agents; furthermore, their volumetric resolutions are limited to around 1 mm^3 (Tai *et al.*, 2003) and 1–0.04 mm^3 (Acton & Kung, 2003; Beekman *et al.*, 2005; Madsen, 2007; Van der Have *et al.*, 2007), respectively.

The X-ray fluorescent technique using synchrotron radiation at the first stage was employed in planar mode to evaluate very low contents of medium- or high-atomic-number trace elements about picograms (Iida & Gohshi, 1991). However, this method is usually limited to scanning either the surface of the object or thin slices of samples with a perpendicular X-ray beam. The X-ray fluorescent computed tomography (XFCT) method bypasses this restriction. Hogan *et al.* (1991) theoretically discussed this approach and we were the first to implement it by using synchrotron radiation (Takeda *et al.*, 1996). Excellent XFCT images were obtained with phantoms containing iodine (Takeda *et al.*, 1997), with endogenous iodine in an excised human thyroid gland (Rust & Weigelt, 1998; Takeda *et al.*, 2000, 2001), and with non-radioactive iodine-labeled BMIPP in an *ex vivo* heart (Takeda *et al.*, 2002; Thet-Thet-Lwin *et al.*, 2007, 2008). The remarkable sensitivity of this method, which is adequate to image biological material with non-radioactive iodine-labeled agents, inspired us to upgrade our XFCT to *in vivo* studies (Takeda *et al.*, 2004). Earlier, we imaged rat brains *in vivo* at 1 mm in-plane spatial resolution; however, image quality was poor owing to the small number of projections (Takeda, 2005). Here, we report the results from our upgraded XFCT system wherein the scanning technique was improved so that it did not scan areas outside the object. We also discuss the potential of the method in certain researches, and enumerate the significance of the spatial resolution in *in vivo* and *ex vivo* applications.

2. Methods and materials

2.1. X-ray fluorescent CT system

Our XFCT system consists of a silicon (220) double-crystal monochromator, an X-ray slit system for determining the size

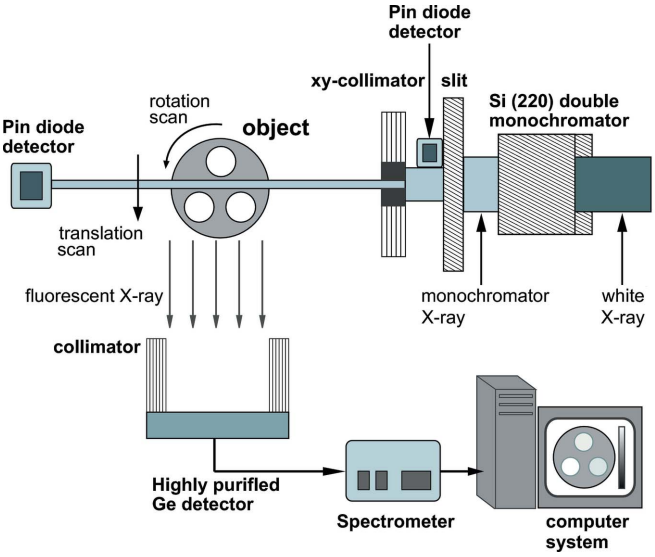

Figure 1
Schematic diagram of the X-ray fluorescent CT system.

of the beam, a subject positioning/scanning table, a high-purity germanium (HPGe) detector (IGRET, EG&G Ortec, USA) equipped with an X-ray collimator, and two pin-diode detectors positioned at 0° (Thet-Thet-Lwin *et al.*, 2007) (Fig. 1). The HPGe detector, placed perpendicular to the incident X-ray beam to reduce stray radiation, registers fluorescent X-rays emitted isotropically from the subject along the path of the beam. We positioned the surface of the detector at 90 mm from the subject, when it was operated in a photon-counting mode with an energy resolution of about 230 eV at the iodine $K\alpha$ line of 27.5 keV (Takeda *et al.*, 2004). Two pin-diode detectors, operated in the current integration mode with pico-ammeters (486, Keithley, USA), monitored the intensity of the incident monochromatic X-rays, which declined exponentially with the decrease of the accelerator ring current, and the transmitted X-ray intensity through the subject for imaging the X-ray transmission CT (XTCT). The experiments were carried out at the bending-magnet beamline of the Photon Factory Advanced Ring in Tsukuba, Japan. The synchrotron storage ring was operated at 6.5 GeV energy. The white X-ray beam from the storage ring was monochromated at 37 keV X-ray energy. The photon flux in front of the objects was approximately 8×10^7 photons mm^{-2} s^{-1} at 35 mA ring current.

2.2. Scanning protocols

The head of an anesthetized mouse was scanned in either 1 mm or 0.5 mm translation steps, and 6° and 4.5° rotation steps over a range of 180°, respectively. Since the translation step and projection number must increase to obtain the XFCT image with 0.5 mm in-plane spatial resolution, the data acquisition time was shortened to 3 s instead of 5 s with 1 mm in-plane spatial resolution image. We selected these steps and data acquisition times to limit the duration of anesthesia to less than 1.5 h. The beam width and height was set at 1 mm and 0.2 mm, or 0.5 mm and 0.5 mm (horizontally and vertically), respectively. To examine the feasibility of acquiring XFCT images with a little more high spatial resolution, *viz.* 0.5 mm and 0.25 mm, we obtained *ex vivo* images of the brain. Table 1 summarizes the data acquisition protocol, the beam cross section and the acquisition time. Here, 1 mm, 0.5 mm and 0.25 mm in-plane spatial resolutions correspond to 1 mm, 0.5 mm and 0.25 mm translation scan steps, respectively. Using the point spread function from a phantom, the image with 0.25 mm in-plane spatial resolution had a true resolution of about 0.27 mm, as in a previous study (Yu *et al.*, 2000).

Table 1
Data acquisition protocol.

	In vivo 1	*In vivo* 2	*Ex vivo* 1	*Ex vivo* 2
Incident X-ray beam collimation				
Incident beam width (mm)	1.0	0.5	0.5	0.25
Incident beam height (mm)	0.2	0.5	0.5	0.5
X-direction scan step (mm)	1.0	0.5	0.5	0.25
Data acquisition time per point (s)	5.0	3.0	3.0	7.0
Number of CT projections acquired	30	40	40	60
Object size (mm)	∼20	∼20	10	10

2.3. Image reconstruction

We reconstructed the XFCT and XTCT images after correcting for the decrement in the intensity of the incident monochromatic X-rays. Using the net counts under the characteristic iodine $K\alpha$ fluorescent X-ray spectral lines at each projection, we reconstructed the XFCT images algebraically, including a correction for the incident beam attenuation and the emitted fluorescent X-ray with the XTCT data (Yuasa *et al.*, 1997). The XTCT image was reconstructed *via* a filtered back-projection method with a Shepp and Logan filter. Then we superimposed the XFCT image on the XTCT image to define the level of cerebral perfusion in different anatomical structures; since both images were obtained simultaneously using a pencil beam, as shown in Fig. 1, geometrical matching was quite easy (Zeniya *et al.*, 2001).

2.4. Preparation of the mice and their autoradiogram

We obtained images from seven living mice, weighing 20–24 g with heads of diameter ∼20 mm, after we employed a 10 mm-diameter contrast-resolution acrylic phantom to assess the contrast resolution in an *ex vivo* brain. The phantom consisted of three 5 mm-diameter axial cylindrical channels filled with three different iodine solutions, their concentrations ranging from 0.005 to 0.1 mg ml^{-1}.

We used non-radioactive ^{127}I-labeled *N*-isopropyl-*p*-iodoamphetamine (^{127}I-IMP containing 0.38 mg iodine) for *in vivo* imaging of the brain, while radioactive ^{123}I-IMP is commonly employed to evaluate cerebral perfusion in clinical SPECT studies (Winchell *et al.*, 1980; Hank *et al.*, 1990; Devous, 2000). Imaging started 5 min after intravenously injecting ^{127}I-IMP

into a mouse anesthetized with pentobarbital; this dose is similar to that used by others in animal SPECT studies (Acton & Kung, 2003). The head of the mouse was set in the vertical direction to the pencil beam, fixed by an animal head holder to suppress any movement. Since the amount of IMP in the brain declined gradually with the approximate half-life time of 1.5 h, we surgically removed the brain of another mouse for the *ex vivo* experiments 5 min after intravenously injecting the ^{127}I-IMP and fixed it in the formalin. Then it was set within a formalin-filled acrylic cell, and imaged by XFCT at 0.5 mm and 0.25 mm in-plane spatial resolution. The XFCT image of the phantom was obtained at 0.25 mm in-plane spatial resolution.

For comparison, we obtained autoradiograms with radioactive ^{125}I-IMP from two other mice. Their brains were removed surgically 5 min after injecting ^{125}I-IMP (15 kBq kg^{-1}), fixed in formalin, and cut into 0.02 mm slices. These samples were exposed on an imaging plate (IP) for 48 h, and the plate was read by a BAS 5000 (Fuji) IP reader at 0.05 mm scan steps and 16-bit depths.

The Medical Committee for the Use of Animals in Research of the University of Tsukuba approved our experiment that fully conformed to the guidelines of the American Physiological Society.

2.5. Quantitative evaluation of the XFCT image

The signal-to-noise ratio (SNR) of the XFCT images was calculated using the following equation: SNR = $(I_i - I_b)/I_n$, wherein I_i is the averaged count on the cortex and thalamus, I_b is the background count on the soft tissue region of skull, and I_n is the standard deviation of the averaged count in the surrounding background. The background region was the skull for the *in vivo* XFCT image, while the formalin solution in the cell served as such for the *ex vivo* XFCT image.

All values were expressed as mean ± standard deviation. The differences between the mean counts of cortex and thalamus were analyzed using the Student's unpaired t test, wherein a probability p value of less than 0.05 denoted a statistically significant difference. We undertook a linear regression analysis to assess the correlation between the fluorescent X-ray counts and iodine concentrations.

3. Results

3.1. Phantom experiments

Using a contrast-resolution phantom, we confirmed that the XFCT could visualize a 0.005 mg ml^{-1} iodine solution at 0.25 mm in-plane spatial resolution and 0.5 mm slice thickness (Fig. 2*a*). There was an excellent linear correlation between the fluorescent X-ray counts per pixel in the XFCT image and the iodine concentration (Fig. 2*b*). From this graph we estimated the iodine concentration in the brain for a given image count.

3.2. *In vivo* XFCT imaging

Both the *in vivo* XFCT image at a 1 mm and at a 0.5 mm in-plane spatial resolution revealed the cerebral perfusion of

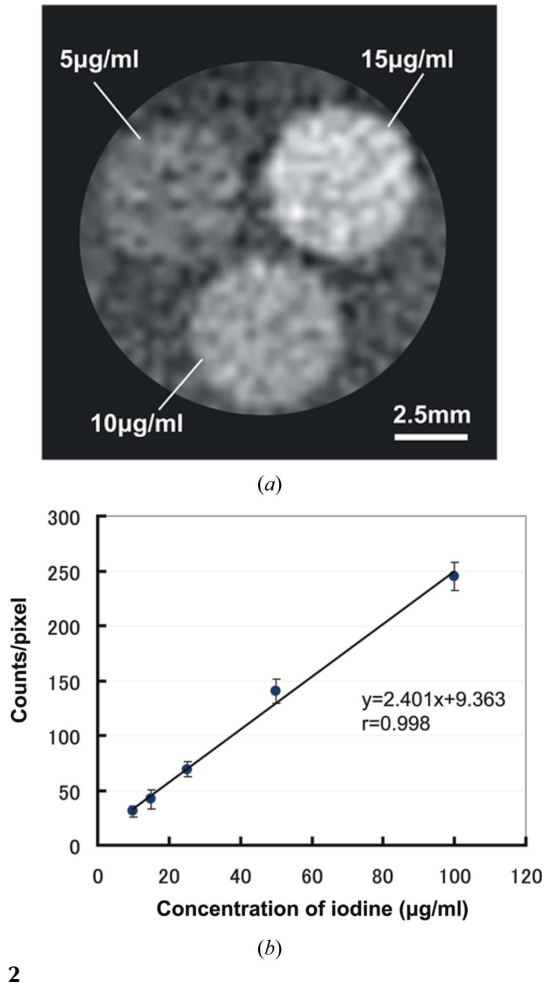

Figure 2
XFCT image of 10 mm-diameter acrylic phantoms filled with 5, 10 and 15 μg ml^{-1} iodine solution obtained at 0.25 mm in-plane spatial resolution (*a*). There is a good linear correlation between the fluorescent X-ray count per pixel (y) and the iodine concentration (x).

^{127}I-IMP throughout the brain of the mouse (Fig. 3), whereas absorption-contrast XTCT discriminated only between the soft tissue and the bony structures of the skull. Cerebral perfusion in the cortex and hippocampus was more clearly visualized in the 0.5 mm in-plane spatial resolution XFCT image than in the 1 mm in-plane resolution image, while the anatomical features of the skull bone were clearly demonstrated by XTCT. Furthermore, the superimposed image (XFCT and XTCT) demonstrated the correspondence between anatomical features and cerebral perfusion. The measured SNR of the XFCT image in cerebral cortex, hippocampus and thalamus was about 12.3, 11.7 and 21.1, respectively (Table 2). We calculated that the mouse experienced a radiation-absorbed dose of about 0.36 Gy for the XFCT imaging experiment.

3.3. *Ex vivo* XFCT imaging

XFCT clearly imaged the formalin-fixed brain in an acrylic cell both at a 0.5 mm and a 0.25 mm in-plane spatial resolution, while, in contrast, the XTCT image discriminated only the margin of the acrylic cell, and failed to distinguish the

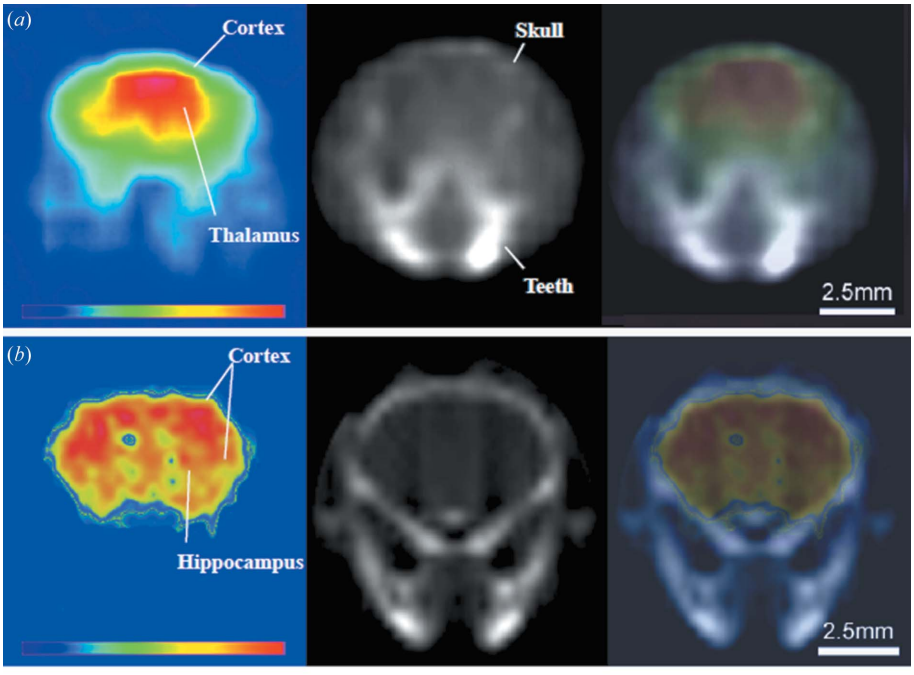

Figure 3
In vivo XFCT, XTCT and superimposed images of normal mouse brains obtained at 1 mm (*a*) and 0.5 mm (*b*) in-plane spatial resolution. The XFCT image visualized cerebral perfusion in the cortex and thalamus at 1 mm in-plane spatial resolution, and detailed cerebral perfusion in the cortex and hippocampus at 0.5 mm in-plane spatial resolution. The XTCT image demonstrates only the margin of the head and skull bone; however, the image quality at 0.5 mm in-plane spatial resolution was excellent. The superimposed image depicts the correspondence between anatomical features and functional state.

Table 2
Signal-to-noise ratio (SNR) of the XFCT images.

	SNR			
	In vivo 1	*In vivo* 2	*Ex vivo* 1	*Ex vivo* 2
Cortex	12.3 + 1.5	13.8 + 1.6	6.3 + 0.4	7.4 + 0.6
Hippocampus	–	11.7 + 1.7	8.1 + 0.6	6.5 + 0.7
Thalamus	21.1 + 1.4†	–	16.2 + 1.0†	16.8 + 1.0†

† Significant difference from other regions with $p < 0.05$.

brain from its surrounding solution (Fig. 4). An *ex vivo* XFCT image was obtained in the same slice level; however, the XFCT image at 0.25 mm in-plane spatial resolution clearly differentiated the detailed structures, such as the cortex, hippocampus and thalamus, with almost the same quality as an autoradiogram with radioactive ^{125}I-IMP.

The IMP dose was approximately 27.3, 23.8 and 50.3 μg g^{-1} in the cortical surface, hippocampus and thalamus, respectively. The SNR in the cerebral cortex was about 7.4 for the 0.25 mm in-plane spatial resolution and 6.3 for the 0.5 mm in-plane spatial resolution (Table 2).

4. Discussion

We obtained good *in vivo* XFCT images of cerebral perfusion in the brain of the mouse at 1 mm and 0.5 mm in-plane spatial resolution with a SNR value higher than 11.7; the anatomical structures of the mouse's brain were easily distinguished in the latter image. Superimposed images of XFCT and XTCT revealed the correspondence between anatomical structures and the level of cerebral perfusion. *Ex vivo* XFCT images with in-plane spatial resolutions of 0.5 mm and 0.25 mm allowed us to distinguish critical areas, such as the cortex, hippocampus and thalamus. The quality of the XFCT image with 0.25 mm in-plane spatial resolution was excellent, similar to the autoradiogram that we obtained with ^{125}I-IMP.

These results suggest that the XFCT technique can generate images of the distribution of a non-radioactive iodine-labeled agent in a volumetric resolution of less than 0.2 mm^3 (0.2–0.03 mm^3). Since volumetric resolution is limited to about 1 mm^3 in micro-PET (Tai *et al.*, 2003) and 1.0–0.04 mm^3 in micro-SPECT (Acton & Kung, 2003; Beekman *et al.*, 2005; Van der Have *et al.*, 2007), the *in vivo* XFCT technique could yield images of a volume about ten times smaller than with micro-PET, and almost comparable with or better

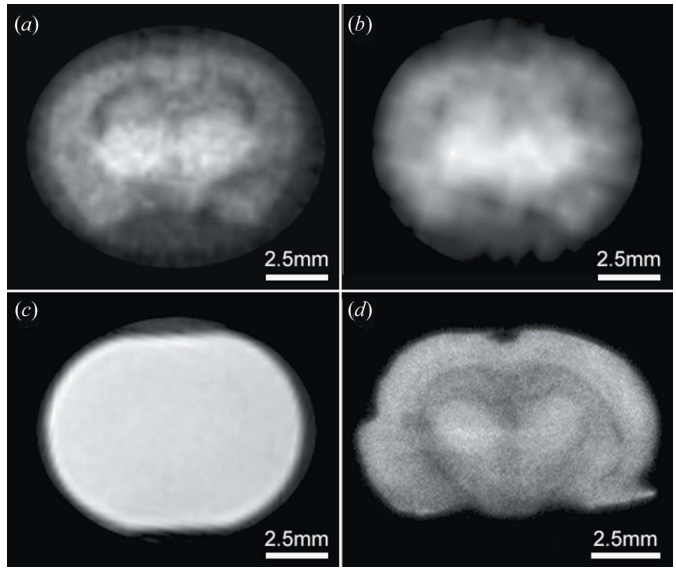

Figure 4
XFCT image of formalin-fixed (*ex vivo*) mouse brain set within an acrylic cell filled with formalin (*a*, *b*, *c*), and autoradiogram with ^{125}I-IMP (*d*). Cerebral perfusion in the cortex, hippocampus and thalamus are well depicted in the 0.25 mm in-plane spatial resolution image (*a*), whereas the hippocampus was not clearly separated from the thalamus in the 0.5 mm in-plane spatial resolution image (*b*). The XTCT image shows only the margin of the acrylic cell's wall, while the inner area including the brain and formalin solution is homogeneous (*c*). Autoradiogram of the brain of a mouse injected with ^{125}I-IMP (*d*).

than those with micro-SPECT. Even recently the U-SPECT-II system enabled an *in vivo* mouse image demonstration at 0.35 mm spatial resolution (Van der Have *et al.*, 2007). Extrapolating from our findings with *ex vivo* XFCT imaging, we suggest that *in vivo* XFCT images might be obtained at a high in-plane spatial resolution of 0.25 mm.

Thus, we conclude that the XFCT offers an excellent capability to image functional information with almost comparable with or higher spatial resolution than other imaging modalities employing a radioactive agent. Employing a non-radioactive labeling agent, as in XFCT, has advantages for biomedical experiments since it does not entail radiation exposure to researchers, and preparing the non-radioactive label agent is easy without specific radiation protection, and the pathological examination after XFCT image acquisition can easily be performed outside of radio-isotope usage areas.

5. Present limitations and future plans

In our *in vivo* XFCT imaging we selected in-plane spatial resolutions of 1 mm or 0.5 mm to ensure that the data acquisition time did not exceed about 1.5 h. Obtaining images with 0.25 mm in-plane spatial resolution will lengthen the acquisition time to about 6 h, *i.e.* four times longer to improve the spatial resolution by half. This period is untenable; thus, to attain such high-resolution images we need a high-speed data acquisition system to ensure a short period of anesthesia. In our present experiment the HPGe detector was geometrically positioned 90 mm from the animal to reduce the dead-time caused by saturation of the detector; thereby the detectable fluorescent X-ray count from the animal is limited to only 0.02% in radiation solid angle by the slit aperture's detection area of 20 mm^2 (10 mm horizontal and 2 mm vertical). The data acquisition time is expected to be about 36 times faster by placing the detector at a distance of 15 mm [increased gain: $36 = (90\ mm/15\ mm)^2$], so we need to improve its efficiency. Ideally, using a high-speed XFCT system with a high-count-rate detector and realising an optimal data-transfer rate (1 s per point in the present system), we could acquire XFCT images with spatial resolutions of 1 mm, 0.5 mm or 0.25 mm in about 2 min, 8 min or 32 min, respectively. Recently, instead of the pencil-beam scanning technique as first-generation CT, we succeeded in obtaining an XFCT image of the phantom and *ex vivo* brain using a sheet beam as the next-generation CT (Huo *et al.*, 2008). By using this sheet-beam technique with a multi-detector system, where an image is obtained only by rotation of the object without an x-line translation scan, then the data acquisition time will be shortened significantly.

In *in vivo* XFCT imaging, the intracranial position of the mouse could not be set at the same slice because the line detector to monitor the position was not equipped in our preliminary system. Thus the level of trans-axial slice was not the same as in Figs. 3(a) and 3(b). We are designing a line detector to monitor the scanning position.

We are convinced that the 0.36 Gy radiation-absorbed dose given to the mouse is not excessive for this kind of measurement, because the animal can tolerate it in a limited volume and it is only about ten-fold larger than that given to patients in clinical X-ray CT studies. In the ideal high-speed XFCT system, this dose will fall by 1/36 for the pencil-beam scanning technique and 1/190 in the sheet-beam technique (45 mm detector–object distance). By realising such an ideal system, we are also improving the scanning technique and the data transfer procedure to the computer, and also planning to improve the detector system with high-count-rate capability.

6. Conclusions

Our experimental results presented here demonstrate that *in vivo* XFCT images of cerebral perfusion can be undertaken without using radioactive agents at a volumetric resolution of less than 0.2 mm^3. We have confirmed that XFCT might afford a novel molecular-imaging technique with high spatial resolution, with an optical XFCT system that is unavailable in other functional imaging techniques.

We thank Xiaowei Chang PhD, Naoki Sunaguchi MS, Taichi Kuroe MS, Seita Nasukawa MS and Takeshi Murakami MS, Mr Hidenori Sato and Mr Kouzou Kobayashi for their technical support, Dr Avril D. Woodhead for reviewing the manuscript, and Nihon Medi-Physics for supplying IMP. This research was partially supported by a Grant-In-Aid for Scientific Research (No. 19390313) from the Japanese Ministry of Education, Science and Culture, and performed under the auspices of the National Laboratory for High Energy Physics (2007G643).

References

Acton, P. D. & Kung, H. F. (2003). *Nucl. Med. Biol.* **30**, 889–895.
Beekman, F. J., Van der Have, F., Vastenhouw, B., Van der Linden, A. J. A., Van Rijk, P. P., Burbach, J. P. H. & Smidt, M. P. (2005). *J. Nucl. Med.* **46**, 1194–1200.
Chatziioannou, A. F. (2002). *Eur. J. Nucl. Med.* **29**, 98–114.
Devous, M. D. (2000). *Functional Cerebral SPECT and PET Imaging*, edited by R. L. Van Heertum and R. S. Tikofsky, pp. 3–22. Philadelphia: Lippincott Williams and Wilkins.
Hank, F. K., Ohmomo, Y. & Kung, M. P. (1990). *Semi. Nucl. Med.* **20**, 290–302.
Herschman, H. R. (2003). *Science*, **302**, 605–608.
Hogan, J. P., Gonsalves, R. A. & Krieger, A. S. (1991). *IEEE Trans. Nucl. Sci.* **38**, 1721–1727.
Huo, Q., Yuasa, T., Akatsuka, T., Takeda, T., Wu, J., Thet-Thet-Lwin, Hyodo, K. & Dilmanian, F. A. (2008). *Opt. Lett.* **30**, 2494–2496.
Iida, A. & Gohshi, Y. (1991). *Handbook on Synchrotron Radiation*, Vol. 4, edited by S. Ebashi, M. Koch and E. Rubenstein, pp. 307–348. Amsterdam: North-Holland.
Madsen, M. T. (2007). *J. Nucl. Med.* **48**, 661–673.
Rust, G. F. & Weigelt, J. (1998). *IEEE Trans. Nucl. Sci.* **45**, 75–88.
Tai, Y. C., Chatziioannou, A. F., Yang, Y., Silverman, R. W., Meadors, K., Siegel, S., Newport, D. F., Stickel, J. R. & Cherry, S. R. (2003). *Phys. Med. Biol.* **48**, 1519–1537.
Takeda, T. (2005). *Nucl. Instrum. Methods Phys. Res. A*, **548**, 38–46.
Takeda, T., Akiba, M., Yuasa, T., Akatsuka, T., Kazama, M., Hoshino, Y., Hyodo, K., Dilmanian, F. A., Akatsuka, T. & Itai, Y. (1996). *Proc. SPIE*, **2708**, 685–695.

Takeda, T., Momose, A., Yu, Q., Yuasa, T., Dilmanian, F. A., Akatsuka, T. & Itai, Y. (2000). *Cell. Mol. Biol.* **46**, 1077–1088.
Takeda, T., Tsuchiya, Y., Kuroe, T., Zeniya, T., Wu, J., Thet-Thet-Lwin, Yashiro, T., Yuasa, T., Hyodo, K., Matsumura, K., Dilmanian, F. A., Itai, Y. & Akatsuka, T. (2004). *AIP Conf. Proc.* **705**, 1320–1323.
Takeda, T., Yu, Q., Yashiro, T., Zeniya, T., Wu, J., Hasegawa, Y., Thet-Thet-Lwin, Hyodo, K., Yuasa, T., Dilmanian, F. A., Akatsuka, T. & Itai, Y. (2001). *Nucl. Instrum. Methods Phys. Res. A*, **467–468**, 1318–1321.
Takeda, T., Yuasa, T., Hoshino, A., Akiba, M., Uchida, A., Kazama, M., Hyodo, K., Dilmanian, F. A., Akatsuka, T. & Itai, Y. (1997). *Proc. SPIE*, **3149**, 160–172.
Takeda, T., Zeniya, T., Wu, J., Yu, Q., Thet-Thet-Lwin, Tsuchiya, Y., Rao, D. V., Yuasa, T., Yashiro, T., Dilmanian, F. A., Itai, Y. & Akstsuka, T. (2002). *Proc. SPIE*, **4503**, 299–311.
Thet-Thet-Lwin, Takeda, T., Wu, J., Huo, Q., Yuasa, T., Hyodo, K. & Akatsuka, T. (2008). *J. Synchrotron Rad.* **15**, 528–531.
Thet-Thet-Lwin, Takeda, T., Wu, J., Sunaguchi, N., Murakami, T., Mouri, S., Nasukawa, S., Huo, Q., Yuasa, T., Hyodo, K. & Akatsuka, T. (2007). *J. Synchrotron Rad.* **14**, 158–162.
Van der Have, F., Vastenhouw, B. & Beekman, F. J. (2007). *J. Nucl. Med.* **48** (Suppl. 2), 47P.
Winchell, H. S., Horst, W. D., Braum, W. H., Oldendorf, R., Hattner, R. & Parker, H. (1980). *J. Nucl. Med.* **21**, 947–952.
Yang, Y., Tai, Y. C., Siegel, S., Newport, D. F., Bai, B., Li, Q., Leahy, R. M. & Cherry, S. R. (2004). *Phys. Med. Biol.* **49**, 2527–2545.
Yu, Q., Takeda, T., Yashiro, T., Yuasa, T., Hasegawa, Y., Zeniya, T., Hyodo, K., Wu, J., Dilmanian, F. A., Akatsuka, T. & Itai, Y. (2000). *Med. Imag. Tech.* **18**, 805–816.
Yuasa, T., Akiba, M., Takeda, T., Kazama, M., Hoshino, A., Watanabe, Y., Hyodo, K., Dilmanian, F. A., Akatsuka, T. & Itai, Y. (1997). *IEEE Trans. Nucl. Sci.* **44**, 54–62.
Zeniya, T., Takeda, T., Yu, Q., Hasegawa, Y., Hyodo, K., Yuasa, T., Hiranaka, Y., Itai, Y. & Akatsuka, T. (2001). *Nucl. Instrum. Methods Phys. Res. A*, **467–468**, 1326–1328.